

One-step Iterative Estimation of Effective Atomic Number and Electron Density for Dual Energy CT

QIAN WANG¹, HUIQIAO XIE², TONGHE WANG², JUSTIN ROPER¹, HAO GAO³, ZHEN TIAN⁴, XIANGYANG TANG⁵, JEFFREY D. BRADLEY¹, TIAN LIU⁶, and XIAOFENG YANG¹

¹Department of Radiation Oncology and Winship Cancer Institute, Emory University, Atlanta, GA, 30322, USA

²Department of Medical Physics, Memorial Sloan Kettering Cancer Center, New York, NY, USA

³Department of Radiation Oncology, University of Kansas Medical Center, Kansas City, MO, USA

⁴Department of Radiation & Cellular Oncology, University of Chicago, Chicago, IL, 60637, USA

⁵Department of Radiology and Imaging Sciences and Winship Cancer Institute, Emory University, Atlanta, GA, 30322, USA

⁶Department of Radiation Oncology, Icahn School of Medicine at Mount Sinai, New York, NY, 10029 USA

Corresponding author: Xiaofeng Yang (e-mail: xiaofeng.yang@emory.edu).

This research was supported in part by the National Institutes of Health under Award Number R01CA272991.

ABSTRACT Dual-energy computed tomography (DECT) is a promising technology that has shown a number of clinical advantages over conventional X-ray CT, such as improved material identification, artifact suppression, etc. For proton therapy treatment planning, besides material-selective images, maps of effective atomic number (Z) and relative electron density to that of water (ρ_e) can also be achieved and further employed to improve stopping power ratio accuracy and reduce range uncertainty. In this work, we propose a one-step iterative estimation method, which employs multi-domain gradient L_0 -norm minimization, for Z and ρ_e maps reconstruction. The algorithm was implemented on GPU to accelerate the predictive procedure and to support potential real-time adaptive treatment planning. The performance of the proposed method is demonstrated via both phantom and patient studies.

INDEX TERMS Dual energy CT, effective atomic number estimation, electron density estimation, L_0 -norm minimization, multi-domain based regularization.

I. INTRODUCTION

COMPARED with traditional radiation therapy, proton therapy is superior in treatment of complex and recurrent tumors with maximized normal tissue and organ at risk (OAR) sparing beyond the target. This can effectively reduce the radiation toxicity and side effects [1]. However, proton therapy suffers from the range uncertainty issue and requires accurate dose calculation for treatment planning [2]. Conventionally, either analytical or Monte Carlo dose calculation algorithms employ the stopping power ratio (SPR) or mass density that is obtained with the stoichiometric relationships from the Hounsfield units (HU) of the single energy simulation CT [3]–[6]. This category of methods relies on linear fitting of the SPR and mass density as a function of the planning CT HU numbers. It is susceptible to noise and fitting errors. In addition, HU ambiguity, i.e., in fact that different materials can have the same HU value is another issue in determination of the SPR and mass density. Therefore, a 3% margin is typically reserved for the uncertainty of calculated

proton range [2].

Dual-energy computed tomography (DECT) has been employed to avoid HU ambiguity and improve SPR accuracy [7]–[9]. In general, a two-step workflow is followed: material decomposition and generating maps of effective atomic number (Z) and relative electron density to that of water (ρ_e). With Z and ρ_e , SPR can be further calculated [10]–[12]. Material decomposition of DECT is typically an ill-posed inverse problem. During the material decomposition calculation process, the noise level can be substantially magnified, which further affects both spatial resolution and contrast. As a consequence, fine structures and low-contrast details may be submerged by noise, on top of the decreased accuracy of material decomposition. To solve this problem, image based, projection based, and iterative methods have been proposed. For image-based methods, decomposition is performed in reconstructed image domain by following a linear pattern [13]. Projection based methods require geometrical consistency and perform decomposition before reconstruction, i.e., in

projection domain [14], [15]. Iterative methods are proposed based on statistical models and nonlinear optimizations [16]–[19]. By introducing nonlinear relationship and smoothness mechanism, both beam-hardening artifacts and noise can be effectively suppressed. For the second step, the calculation of Z and ρ_e is an independent close-form process, which is separated from material decomposition [20]–[22]. Thus, the final results of Z and ρ_e highly depend on the image quality of decomposed material images. Meanwhile, because of the ill-posedness and deficiency of smoothness mechanism, noise can be amplified again in the step of Z and ρ_e generation.

One popular smoothness strategy belongs to compressed sensing, which searches for sparse description in some specific domain. The most typical representatives are Tikhonov regularization (L_2 -norm of image gradient) [23] and TV regularization (L_1 -norm of image gradient) [24]–[26]. Different from Tikhonov and TV regularization penalizing gradient magnitude, gradient L_0 -norm punishes the gradient existence, which has the strongest capability of sparsity representation and is superior in edge preservation and noise suppression. However, the counting function of non-zero gradient leads to an NP-hard problem, which dramatically increases the solution difficulty [27], [28]. To improve the feasibility, an approximation method was proposed by Xu et al [29], [30].

In this work, we develop an iterative one-step decomposition method with gradient L_0 -norm minimization to estimate the effective atomic number and electron density from dual energy CT. Different from the aforementioned two-step approach, the established optimization model can obtain material composition, Z and ρ_e maps simultaneously. Moreover, we introduce multi-domain regularizers for each searched-for variables. Thus, during the alternative solution process, the noise magnification problem can be consistently suppressed. Especially, gradient L_0 -norm is superior to traditional Tikhonov and TV regularizations in sparse representation and edge preservation, which further benefits noise reduction and fidelity maintenance. The effectiveness and superior performance of the proposed method is demonstrated with both phantom and patient studies.

The remainder of this paper is organized as follows. In section II, we review monoenergetic CT synthesization, Z and ρ_e estimation, and gradient L_0 -norm minimization. Then, we propose a multi-domain regularization based optimization model, and provide the algorithm for one-step estimation of material composition, Z and ρ_e maps. In section III, both phantom and patient studies are performed to verify the effectiveness of the proposed methods. In last section, we discuss some related issues and conclude this paper.

II. METHODS

In this section, the mathematical models of DECT material decomposition and monoenergetic CT synthesization are presented, and the estimation of Z and ρ_e maps and solution process of gradient L_0 norm minimization are briefly reviewed. Then, by incorporating multi-domain gradient L_0

norm minimization, we establish an optimization model with multi-objectives. We also derive the iterative solution method and summarize the algorithm.

A. SYNTHESIS OF MONOENERGETIC CT IMAGE

The basic assumption of DECT material decomposition is the linear attenuation coefficient (μ) dependence on energy and material can be separated. Typically, there are two explanations, i.e., basis material decomposition and photoelectric/Compton effect based decomposition. For the first scenario, let f_1 and f_2 represent the composition images of two basis materials, E_L and E_H low and high energies employed for clinic DECT scan, and $\mu_1(\cdot)$ and $\mu_2(\cdot)$ the corresponding linear attenuation coefficients of the basis materials f_1 and f_2 under some specific energy setting. Thus, the achieved linear attenuation coefficient images of DECT can be described as,

$$\mu(E_L) = f_1\mu_1(E_L) + f_2\mu_2(E_L), \quad (1a)$$

$$\mu(E_H) = f_1\mu_1(E_H) + f_2\mu_2(E_H). \quad (1b)$$

After solving f_1 and f_2 from (1a) and (1b), we can synthesize mass attenuation coefficient (μ/ρ) image under some preferred monochromatic energy, such as E_1 and E_2 as follows,

$$\frac{\mu(E_1)}{\rho} = f_1 \frac{\mu_1(E_1)}{\rho_1} + f_2 \frac{\mu_2(E_1)}{\rho_2}, \quad (2a)$$

$$\frac{\mu(E_2)}{\rho} = f_1 \frac{\mu_1(E_2)}{\rho_1} + f_2 \frac{\mu_2(E_2)}{\rho_2}, \quad (2b)$$

where ρ_1 and ρ_2 are the mass density of the two basis materials. In this study, we use energy levels at 50 keV (E_1) and 200 keV (E_2), at which the photoelectric effect and the Compton effect are respectively the dominant X-ray interactions with matter.

B. ESTIMATION OF ELECTRON DENSITY AND EFFECTIVE ATOMIC NUMBER

For the energy range used in clinical CT, coherent (Rayleigh) scattering can often be neglected for standard body tissues. Thus, the mass-attenuation coefficient can be attributed to photoelectric absorption and incoherent (Compton) scattering, i.e.,

$$\frac{\mu(E)}{\rho} = a_p\psi_p(E) + a_c\psi_c(E),$$

where $\psi_p(E)$ and $\psi_c(E)$ are the energy dependencies of photoelectric absorption and Compton scattering, and a_p and a_c the characteristic constants of the material. The photoelectric term can be approximated by

$$a_p\psi_p(E) \simeq \rho_e C_p \frac{Z^m}{E^n},$$

where ρ_e is the electron density, Z the effective atomic number, and constants $C_p = 9.8 \times 10^{-24}$, $m = 3.8$ and $n = 3.2$ [22], [31]. The Compton scattering part can be

represented by electron density and the total Klein-Nishina cross-section, i.e., $a_c = \rho_e$ and

$$\psi_c(E) = KN(\gamma) = C_0 \left\{ \frac{1+\gamma}{\gamma^2} \left[\frac{2(1+\gamma)}{1+2\gamma} - \frac{1}{\gamma} \ln(1+2\gamma) \right] + \frac{1}{2\gamma} \ln(1+2\gamma) - \frac{1+3\gamma}{(1+2\gamma)^2} \right\},$$

where $\gamma = \frac{E}{510.975 \text{ keV}}$, $C_0 = 2\pi r_0^2$ and $r_0 = 2.818 \times 10^{-13} \text{ cm}$ is the classical electron radius. Thus, (2a) and (2b) can also be described as,

$$\frac{\mu(E_1)}{\rho} = \rho_e \left(C_p \frac{Z^m}{E_1^n} + \psi_c(E_1) \right), \quad (3a)$$

$$\frac{\mu(E_2)}{\rho} = \rho_e \left(C_p \frac{Z^m}{E_2^n} + \psi_c(E_2) \right). \quad (3b)$$

By rewriting (3a) and (3b) as follows,

$$(\psi_c(E_1)E_1^n - \psi_c(E_2)E_2^n)\rho_e = \frac{\mu(E_1)}{\rho}E_1^n - \frac{\mu(E_2)}{\rho}E_2^n, \quad (4a)$$

$$C_p \left(\frac{\mu(E_1)}{\rho} \frac{1}{E_2^n} - \frac{\mu(E_2)}{\rho} \frac{1}{E_1^n} \right) Z^m = \frac{\mu(E_2)}{\rho} \psi_c(E_1) - \frac{\mu(E_1)}{\rho} \psi_c(E_2), \quad (4b)$$

we can easily obtain Z^m and ρ_e .

C. GRADIENT L_0 NORM MINIMIZATION

Sparse optimization is widely used in image smoothness and noise reduction. One popular preserving regularization is total variation (TV), which penalizes large gradient magnitudes, possibly influencing contrast during smoothing. Another powerful choice is L_0 gradient minimization. As a sparse gradient counting scheme, gradient L_0 -norm minimization is superior to TV in sparse representation without sacrificing contrast magnitude. Assume \tilde{g} is the obtained noisy image and g is the searched-for noise free image. Thus, the optimization model with gradient L_0 -norm minimization can be expressed as [29], [30],

$$\min_g \left\{ \|g - \tilde{g}\|_{L_2}^2 + \lambda C(g) \right\}, \quad (5)$$

where $C(g) = \#\{\mathbf{r} \in \Omega_2 \mid |\partial_x g(\mathbf{r})| + |\partial_y g(\mathbf{r})| \neq 0\}$ represents the gradient L_0 -norm, Ω_2 the 2D spatial image domain, λ a weight directly controlling the smoothness. Noticing (5) is a non-convex problem, we introduce auxiliary variables h_g, v_g and rewrite the optimization model as,

$$\min_g \left\{ \|g - \tilde{g}\|_{L_2}^2 + \lambda C(h_g, v_g) \right\}, \quad (6)$$

s.t. $h_g = \partial_x g$, $v_g = \partial_y g$, where $C(h_g, v_g) = \#\{\mathbf{r} \in \Omega_2 \mid |h_g(\mathbf{r})| + |v_g(\mathbf{r})| \neq 0\}$. Then we relax the constraints and convert (6) to a unconstrained version, i.e.,

$$\min_{g, h_g, v_g} \left\{ \|g - \tilde{g}\|_{L_2}^2 + \lambda C(h_g, v_g) + \beta (\|\partial_x g - h_g\|_{L_2}^2 + \|\partial_y g - v_g\|_{L_2}^2) \right\}, \quad (7)$$

where β is a relaxation parameter controlling the similarity between variables (h_g, v_g) and their corresponding gradients. Further, (7) is split to the following subproblems,

$$\min_g \left\{ \|g - \tilde{g}\|_{L_2}^2 + \beta (\|\partial_x g - h_g\|_{L_2}^2 + \|\partial_y g - v_g\|_{L_2}^2) \right\}, \quad (8a)$$

$$\min_{h_g, v_g} \left\{ \|\partial_x g - h_g\|_{L_2}^2 + \|\partial_y g - v_g\|_{L_2}^2 + \frac{\lambda}{\beta} C(h_g, v_g) \right\}. \quad (8b)$$

For subproblem (8a), we can derive the closed-form solution as follow,

$$g = \mathcal{F}^{-1} \left(\frac{\mathcal{F}(\tilde{g}) + \beta (\mathcal{F}^*(\partial_x) \mathcal{F}(h_g) + \mathcal{F}^*(\partial_y) \mathcal{F}(v_g))}{\mathcal{F}(1) + \beta (\mathcal{F}^*(\partial_x) \mathcal{F}(\partial_x) + \mathcal{F}^*(\partial_y) \mathcal{F}(\partial_y))} \right),$$

where $\mathcal{F}(\cdot)$ and $\mathcal{F}^*(\cdot)$ represent Fast Fourier Transform operator and its complex conjugate. Subproblem (8b) can be spatially decomposed as $\sum_{\mathbf{r} \in \Omega_2} \min_{h_g, v_g} \mathcal{E}(\mathbf{r})$, where $\mathcal{E}(\mathbf{r}) = \left\{ (h_g(\mathbf{r}) - \partial_x g(\mathbf{r}))^2 + (v_g(\mathbf{r}) - \partial_y g(\mathbf{r}))^2 + \frac{\lambda}{\beta} H(|h_g(\mathbf{r})| + |v_g(\mathbf{r})|) \right\}$ and $H(|h_g(\mathbf{r})| + |v_g(\mathbf{r})|)$ is a binary function returning 1 if $|h_g(\mathbf{r})| + |v_g(\mathbf{r})| \neq 0$ and 0 otherwise. The cost function $\mathcal{E}(\mathbf{r})$ reaches its minimum under the condition

$$(h_g(\mathbf{r}), v_g(\mathbf{r})) = \begin{cases} (0, 0), & (\partial_x g(\mathbf{r}))^2 + (\partial_y g(\mathbf{r}))^2 \leq \frac{\lambda}{\beta}, \\ (\partial_x g(\mathbf{r}), \partial_y g(\mathbf{r})), & \text{otherwise.} \end{cases} \quad (9)$$

D. OPTIMIZATION BASED ONE-STEP ESTIMATION OF ELECTRON DENSITY AND EFFECTIVE ATOMIC NUMBER

Inspired by the estimation method of electron density and effective atomic number from synthesized monoenergetic CT image, we propose an optimization model with gradient L_0 -norm minimization as follow,

$$\begin{aligned} & \min_{\substack{f_1, f_2, \\ \rho_e, Z^m}} \left\{ \|f_1 \mu_1(E_L) + f_2 \mu_2(E_L) - \mu(E_L)\|_{L_2}^2 \right. \\ & \quad \left. + \|f_1 \mu_1(E_H) + f_2 \mu_2(E_H) - \mu(E_H)\|_{L_2}^2 \right. \\ & \quad \left. + \|\rho_e \left(C_p \frac{Z^m}{E_1^n} + \psi_c(E_1) \right) - \left(f_1 \frac{\mu_1(E_1)}{\rho_1} + f_2 \frac{\mu_2(E_1)}{\rho_2} \right)\|_{L_2}^2 \right. \\ & \quad \left. + \|\rho_e \left(C_p \frac{Z^m}{E_2^n} + \psi_c(E_2) \right) - \left(f_1 \frac{\mu_1(E_2)}{\rho_1} + f_2 \frac{\mu_2(E_2)}{\rho_2} \right)\|_{L_2}^2 \right. \\ & \quad \left. + \lambda \left(\sum_{i=1}^2 C(f_i) + C(\rho_e) + C(Z^m) \right) \right\}. \quad (10) \end{aligned}$$

By introducing auxiliary variables h_g, v_g ($g = f_1, f_2, \rho_e, Z^m$) and rewrite the optimization model as,

$$\begin{aligned} & \min_{\substack{f_1, f_2, \\ \rho_e, Z^m}} \left\{ \|f_1 \mu_1(E_L) + f_2 \mu_2(E_L) - \mu(E_L)\|_{L_2}^2 \right. \\ & \quad \left. + \|f_1 \mu_1(E_H) + f_2 \mu_2(E_H) - \mu(E_H)\|_{L_2}^2 \right. \\ & \quad \left. + \|\rho_e \left(C_p \frac{Z^m}{E_1^n} + \psi_c(E_1) \right) - \left(f_1 \frac{\mu_1(E_1)}{\rho_1} + f_2 \frac{\mu_2(E_1)}{\rho_2} \right)\|_{L_2}^2 \right. \\ & \quad \left. + \|\rho_e \left(C_p \frac{Z^m}{E_2^n} + \psi_c(E_2) \right) - \left(f_1 \frac{\mu_1(E_2)}{\rho_1} + f_2 \frac{\mu_2(E_2)}{\rho_2} \right)\|_{L_2}^2 \right. \\ & \quad \left. + \lambda \sum_{\substack{g=f_1, f_2, \\ \rho_e, Z^m}} C(h_g, v_g) \right\}, \quad (11) \end{aligned}$$

s.t. $h_g = \partial_x g$, $v_g = \partial_y g$ ($g = f_1, f_2, \rho_e, Z^m$). By relaxing the constraints, (11) is converted to a unconstrained version as follow,

$$\begin{aligned} \min_{\substack{g, h_g, v_g, \\ g=f_1, f_2, \rho_e, Z^m}} & \left\{ \|f_1 \mu_1(E_L) + f_2 \mu_2(E_L) - \mu(E_L)\|_{L_2}^2 \right. \\ & + \|f_1 \mu_1(E_H) + f_2 \mu_2(E_H) - \mu(E_H)\|_{L_2}^2 \\ & + \|\rho_e (C_p \frac{Z^m}{E_1^n} + \psi_c(E_1)) - (f_1 \frac{\mu_1(E_1)}{\rho_1} + f_2 \frac{\mu_2(E_1)}{\rho_2})\|_{L_2}^2 \\ & + \|\rho_e (C_p \frac{Z^m}{E_2^n} + \psi_c(E_2)) - (f_1 \frac{\mu_1(E_2)}{\rho_1} + f_2 \frac{\mu_2(E_2)}{\rho_2})\|_{L_2}^2 \\ & + \beta \sum_{\substack{g=f_1, f_2, \\ \rho_e, Z^m}} (\|\partial_x g - h_g\|_{L_2}^2 + \|\partial_y g - v_g\|_{L_2}^2) \\ & \left. + \lambda \sum_{\substack{g=f_1, f_2, \\ \rho_e, Z^m}} \mathcal{C}(h_g, v_g) \right\}. \quad (12) \end{aligned}$$

We split (12) to the following subproblems,

$$\begin{aligned} \min_{f_1, f_2} & \left\{ \|f_1 \mu_1(E_L) + f_2 \mu_2(E_L) - \mu(E_L)\|_{L_2}^2 \right. \\ & + \|f_1 \mu_1(E_H) + f_2 \mu_2(E_H) - \mu(E_H)\|_{L_2}^2 \\ & + \|(f_1 \frac{\mu_1(E_1)}{\rho_1} + f_2 \frac{\mu_2(E_1)}{\rho_2}) - \rho_e (C_p \frac{Z^m}{E_1^n} + \psi_c(E_1))\|_{L_2}^2 \\ & + \|(f_1 \frac{\mu_1(E_2)}{\rho_1} + f_2 \frac{\mu_2(E_2)}{\rho_2}) - \rho_e (C_p \frac{Z^m}{E_2^n} + \psi_c(E_2))\|_{L_2}^2 \\ & \left. + \beta \sum_{g=f_1, f_2} (\|\partial_x g - h_g\|_{L_2}^2 + \|\partial_y g - v_g\|_{L_2}^2) \right\}, \quad (13a) \end{aligned}$$

$$\begin{aligned} \min_{\rho_e} & \left\{ \|(\psi_c(E_1)E_1^n - \psi_c(E_2)E_2^n)\rho_e \right. \\ & - (\frac{\mu(E_1)}{\rho} E_1^n - \frac{\mu(E_2)}{\rho} E_2^n)\|_{L_2}^2 \\ & \left. + \tilde{\beta} (\|\partial_x \rho_e - h_{\rho_e}\|_{L_2}^2 + \|\partial_y \rho_e - v_{\rho_e}\|_{L_2}^2) \right\}, \quad (13b) \end{aligned}$$

$$\begin{aligned} \min_{Z^m} & \left\{ \|C_p (\frac{\mu(E_1)}{\rho} \frac{1}{E_2^n} - \frac{\mu(E_2)}{\rho} \frac{1}{E_1^n}) Z^m \right. \\ & - (\frac{\mu(E_2)}{\rho} \psi_c(E_1) - \frac{\mu(E_1)}{\rho} \psi_c(E_2))\|_{L_2}^2 \\ & \left. + \tilde{\beta} (\|\partial_x Z^m - h_{Z^m}\|_{L_2}^2 + \|\partial_y Z^m - v_{Z^m}\|_{L_2}^2) \right\}, \quad (13c) \end{aligned}$$

$$\begin{aligned} \min_{\substack{h_g, v_g, \\ g=f_1, f_2, \rho_e, Z^m}} & \left\{ \frac{\lambda}{\beta} \mathcal{C}(h_g, v_g) \right. \\ & \left. + (\|\partial_x g - h_g\|_{L_2}^2 + \|\partial_y g - v_g\|_{L_2}^2) \right\}. \quad (13d) \end{aligned}$$

From subproblem (13a), we can derive the closed-form solutions as follows,

$$\begin{aligned} f_1 = \mathcal{F}^{-1} & \left(\left\{ \mathcal{F} \left[\sum_{i=L, H} \mu_1(E_i) (\mu(E_i) - f_2 \mu_2(E_i)) \right. \right. \right. \\ & + \sum_{j=1}^2 \frac{\mu_1(E_j)}{\rho_1} [\rho_e (C_p \frac{Z^m}{E_j^n} + \psi_c(E_j)) - f_2 \frac{\mu_2(E_j)}{\rho_2}] \left. \right\} \\ & + \beta (\mathcal{F}^*(\partial_x) \mathcal{F}(h_{f_1}) + \mathcal{F}^*(\partial_y) \mathcal{F}(v_{f_1})) \left. \right\} / \left\{ \mathcal{F} \left[\sum_{i=L, H} \mu_1^2(E_i) \right. \right. \\ & \left. \left. + \sum_{j=1}^2 (\frac{\mu_1(E_j)}{\rho_1})^2 \right] + \beta (\mathcal{F}^*(\partial_x) \mathcal{F}(\partial_x) + \mathcal{F}^*(\partial_y) \mathcal{F}(\partial_y)) \right\}, \end{aligned}$$

$$\begin{aligned} f_2 = \mathcal{F}^{-1} & \left(\left\{ \mathcal{F} \left[\sum_{i=L, H} \mu_2(E_i) (\mu(E_i) - f_1 \mu_1(E_i)) \right. \right. \right. \\ & + \sum_{j=1}^2 \frac{\mu_2(E_j)}{\rho_2} [\rho_e (C_p \frac{Z^m}{E_j^n} + \psi_c(E_j)) - f_1 \frac{\mu_1(E_j)}{\rho_1}] \left. \right\} \\ & + \beta (\mathcal{F}^*(\partial_x) \mathcal{F}(h_{f_2}) + \mathcal{F}^*(\partial_y) \mathcal{F}(v_{f_2})) \left. \right\} / \left\{ \mathcal{F} \left[\sum_{i=L, H} \mu_2^2(E_i) \right. \right. \\ & \left. \left. + \sum_{j=1}^2 (\frac{\mu_2(E_j)}{\rho_2})^2 \right] + \beta (\mathcal{F}^*(\partial_x) \mathcal{F}(\partial_x) + \mathcal{F}^*(\partial_y) \mathcal{F}(\partial_y)) \right\}, \end{aligned}$$

where $\mathcal{F}(\cdot)$ and $\mathcal{F}(\cdot)^*$ represent Fast Fourier Transform operator and its complex conjugate. It is noticeable that subproblems (13b) and (13c) are based on the equivalent conversions of (3a) and (3b), i.e., (4a) and (4b). Thus, to eliminate the cost difference caused by the substitution, relaxation parameter β is replaced by a variant $\tilde{\beta}$. Furthermore, electron density ρ_e can be solved from subproblem (13b) by

$$\begin{aligned} \rho_e = \mathcal{F}^{-1} & \left(\left\{ \mathcal{F} \left[(\psi_c(E_1)E_1^n - \psi_c(E_2)E_2^n) (\frac{\mu(E_1)}{\rho} E_1^n - \frac{\mu(E_2)}{\rho} E_2^n) \right. \right. \right. \\ & \left. \left. + \tilde{\beta} (\mathcal{F}^*(\partial_x) \mathcal{F}(h_{\rho_e}) + \mathcal{F}^*(\partial_y) \mathcal{F}(v_{\rho_e})) \right\} / \left\{ \mathcal{F} (\psi_c(E_1)E_1^n \right. \right. \\ & \left. \left. - \psi_c(E_2)E_2^n)^2 + \tilde{\beta} (\mathcal{F}^*(\partial_x) \mathcal{F}(\partial_x) + \mathcal{F}^*(\partial_y) \mathcal{F}(\partial_y)) \right\} \right). \end{aligned}$$

And effective atomic number Z is the m -th root of Z^m , which can be obtained from subproblem (13c) by solving the following quadratic model,

$$\begin{aligned} \min_{Z^m} & \left\{ C_p^2 (\frac{\mu(E_1)}{\rho} \frac{1}{E_2^n} - \frac{\mu(E_2)}{\rho} \frac{1}{E_1^n})^2 + \tilde{\beta} (\partial_x^* \partial_x + \partial_y^* \partial_y) \right\} Z^m \\ & - \left\{ [C_p (\frac{\mu(E_1)}{\rho} \frac{1}{E_2^n} - \frac{\mu(E_2)}{\rho} \frac{1}{E_1^n}) (\frac{\mu(E_2)}{\rho} \psi_c(E_1) - \frac{\mu(E_1)}{\rho} \psi_c(E_2))] \right. \\ & \left. + \tilde{\beta} (\partial_x^* (h_{Z^m}) + \partial_y^* \mathcal{F}(v_{Z^m})) \right\} \|_{L_2}^2 \end{aligned}$$

Subproblem (13d) can be solved by the same strategy for subproblem (8b), i.e., by using (9). Combing all the derivations, the iterative algorithm is summarized in Alg. 1.

III. RESULTS

In this section, we applied the proposed method to two phantom studies and one patient study respectively. The employed phantoms are presented in Fig. 1. All the data were collected by a Siemens SOMATOM Definition Edge scanner using TwinBeam protocols with 120 kV. The x-ray tube current is 210 mA for tissue characterization phantom, 655 mA for multi-energy phantom study and 261mA for patient study. Slice thickness is 0.5 mm with a reconstruction diameter of 500 mm. We compared the proposed method with direct two-step decomposition [32] and estimation method [22]. For visual evaluations, we also magnified local patches and extracted line profiles for detail comparisons. Moreover, for phantom-based quantitative assessments, three numerical image quality measures are employed, i.e., peak signal-to-noise ratio (PSNR) [33], normal mean absolute deviation (NMAD) [34] and structural similarity (SSIM) [35].

A. TISSUE CHARACTERIZATION PHANTOM STUDY

First, the Gammex tissue characterization phantom model 467 (Gammex Inc., Middleton, WI) was scanned, which included 16 insert locations with human reference tissues. In

Algorithm 1 Iterative algorithm of optimization model (10)

Input: images $\mu(E_i)$ ($i = L, H$), energy parameters $\psi_c(E_j)$ and $\mu_j(E_i)$ ($i = L, H, j = 1, 2$), mass attenuation coefficients $\frac{\mu(E_j)}{\rho}$ and $\frac{\mu(E_j)}{\rho}$ ($j = 1, 2$), smoothing weight λ , parameters $\beta^{(0)}, \beta^{(max)}$, and rates τ and κ .

Output: f_1, f_2, ρ_e , and Z^m

Initialization: $f_1^{(0)} = \frac{\mu_2(E_H)\mu(E_L) - \mu_2(E_L)\mu(E_H)}{\mu_1(E_L)\mu_2(E_H) - \mu_1(E_H)\mu_2(E_L)}$, $f_2^{(0)} = \frac{\mu_1(E_L)\mu(E_H) - \mu_1(E_H)\mu(E_L)}{\mu_1(E_L)\mu_2(E_H) - \mu_1(E_H)\mu_2(E_L)}$,

$$\left(\frac{\mu(E_1)}{\rho}\right)^{(0)} = f_1^{(0)} \frac{\mu_1(E_1)}{\rho_1} + f_2^{(0)} \frac{\mu_2(E_1)}{\rho_2}, \left(\frac{\mu(E_2)}{\rho}\right)^{(0)} = f_1^{(0)} \frac{\mu_1(E_2)}{\rho_1} + f_2^{(0)} \frac{\mu_2(E_2)}{\rho_2},$$

$$\rho_e^{(0)} = \frac{\left(\frac{\mu(E_1)}{\rho}\right)^{(0)} E_1^n - \left(\frac{\mu(E_2)}{\rho}\right)^{(0)} E_2^n}{\left(\psi_c(E_1)E_1^n - \psi_c(E_2)E_2^n\right)}, (Z^m)^{(0)} = \frac{\left(\frac{\mu(E_2)}{\rho}\right)^{(0)} \psi_c(E_1) - \left(\frac{\mu(E_1)}{\rho}\right)^{(0)} \psi_c(E_2)}{C_p \left(\left(\frac{\mu(E_1)}{\rho}\right)^{(0)} \frac{1}{E_1^n} - \left(\frac{\mu(E_2)}{\rho}\right)^{(0)} \frac{1}{E_2^n} \right)}, \tilde{\beta}^{(0)} = \tau \beta^{(0)}, k = 0.$$

repeat

With $g^{(k)}$, solve for $h_g^{(k)}$ and $v_g^{(k)}$ ($g = f_1, f_2, \rho_e, Z^m$) in (9).

With $h_g^{(k)}$ and $v_g^{(k)}$, solve for $g^{(k+1)}$ ($g = f_1, f_2, \rho_e, Z^m$) with:

$$f_1^{(k+1)} = \mathcal{F}^{-1} \left(\left\{ \mathcal{F} \left[\sum_{i=L,H} \mu_1(E_i) (\mu(E_i) - f_2^{(k)} \mu_2(E_i)) + \sum_{j=1}^2 \frac{\mu_1(E_j)}{\rho_1} \left[\rho_e^{(k)} \left(C_p \frac{(Z^m)^{(k)}}{E_j^n} + \psi_c(E_j) \right) - f_2^{(k)} \frac{\mu_2(E_j)}{\rho_2} \right] \right\} + \beta^{(k)} (\mathcal{F}(\partial_x)^* \mathcal{F}(h_{f_1}^{(k)}) + \mathcal{F}(\partial_y)^* \mathcal{F}(v_{f_1}^{(k)})) \right\} / \left\{ \mathcal{F} \left[\sum_{i=L,H} \mu_1^2(E_i) + \sum_{j=1}^2 \left(\frac{\mu_1(E_j)}{\rho_1} \right)^2 \right] + \beta^{(k)} (\mathcal{F}(\partial_x)^* \mathcal{F}(\partial_x) + \mathcal{F}(\partial_y)^* \mathcal{F}(\partial_y)) \right\} \right)$$

$$f_2^{(k+1)} = \mathcal{F}^{-1} \left(\left\{ \mathcal{F} \left[\sum_{i=L,H} \mu_2(E_i) (\mu(E_i) - f_1^{(k)} \mu_1(E_i)) + \sum_{j=1}^2 \frac{\mu_2(E_j)}{\rho_2} \left[\rho_e^{(k)} \left(C_p \frac{(Z^m)^{(k)}}{E_j^n} + \psi_c(E_j) \right) - f_1^{(k)} \frac{\mu_1(E_j)}{\rho_1} \right] \right\} + \beta^{(k)} (\mathcal{F}(\partial_x)^* \mathcal{F}(h_{f_2}^{(k)}) + \mathcal{F}(\partial_y)^* \mathcal{F}(v_{f_2}^{(k)})) \right\} / \left\{ \mathcal{F} \left[\sum_{i=L,H} \mu_2^2(E_i) + \sum_{j=1}^2 \left(\frac{\mu_2(E_j)}{\rho_2} \right)^2 \right] + \beta^{(k)} (\mathcal{F}(\partial_x)^* \mathcal{F}(\partial_x) + \mathcal{F}(\partial_y)^* \mathcal{F}(\partial_y)) \right\} \right)$$

$$\left(\frac{\mu(E_1)}{\rho}\right)^{(k+1)} = f_1^{(k)} \frac{\mu_1(E_1)}{\rho_1} + f_2^{(k)} \frac{\mu_2(E_1)}{\rho_2}$$

$$\left(\frac{\mu(E_2)}{\rho}\right)^{(k+1)} = f_1^{(k)} \frac{\mu_1(E_2)}{\rho_1} + f_2^{(k)} \frac{\mu_2(E_2)}{\rho_2}$$

$$\rho_e^{(k+1)} = \mathcal{F}^{-1} \left(\left\{ \mathcal{F} \left[\left(\psi_c(E_1) E_1^n - \psi_c(E_2) E_2^n \right) \left(\left(\frac{\mu(E_1)}{\rho}\right)^{(k)} E_1^n - \left(\frac{\mu(E_2)}{\rho}\right)^{(k)} E_2^n \right) \right] + \tilde{\beta}^{(k)} (\mathcal{F}(\partial_x)^* \mathcal{F}(h_{\rho_e}^{(k)}) + \mathcal{F}(\partial_y)^* \mathcal{F}(v_{\rho_e}^{(k)})) \right\} / \left\{ \mathcal{F} \left(\psi_c(E_1) E_1^n - \psi_c(E_2) E_2^n \right)^2 + \tilde{\beta}^{(k)} (\mathcal{F}(\partial_x)^* \mathcal{F}(\partial_x) + \mathcal{F}(\partial_y)^* \mathcal{F}(\partial_y)) \right\} \right)$$

$$\min_{(Z^m)^{(k+1)}} \left\| \left\{ C_p \left(\left(\frac{\mu(E_1)}{\rho}\right)^{(k)} \frac{1}{E_1^n} - \left(\frac{\mu(E_2)}{\rho}\right)^{(k)} \frac{1}{E_2^n} \right)^2 + \tilde{\beta}^{(k)} (\partial_x^* \partial_x + \partial_y^* \partial_y) \right\} Z^m - \left[C_p \left(\left(\frac{\mu(E_1)}{\rho}\right)^{(k)} \frac{1}{E_1^n} - \left(\frac{\mu(E_2)}{\rho}\right)^{(k)} \frac{1}{E_2^n} \right) \left(\left(\frac{\mu(E_2)}{\rho}\right)^{(k)} \psi_c(E_1) - \left(\frac{\mu(E_1)}{\rho}\right)^{(k)} \psi_c(E_2) \right) \right] + \tilde{\beta}^{(k)} (\partial_x^* (h_{Z^m}^{(k)}) + \partial_y^* \mathcal{F}(v_{Z^m}^{(k)})) \right\|_{L_2}^2$$

$$\beta^{(k)} = \kappa \beta^{(k)}$$

$$\tilde{\beta}^{(k)} = \tau \beta^{(k)}$$

$$k = k + 1$$

until $\beta^{(k)} \geq \beta^{(max)}$

this experiment, the 16 inserts consist of 13 materials. The material list and the reference value of ρ_e and Z are shown in Table 1. The basis materials are chosen as SB3 cortical bone and CT solid water. The decomposed material images and maps of ρ_e and Z are presented in Fig. 2. Results of estimation accuracy are provided in Table 1. Image quality assessments are shown in Table 2.

From Fig. 2, the zoomed-in local patches of the proposed method clearly demonstrated the superior performance in noise suppression and edge preservation, which also can be found from line profile comparisons. Moreover, the results of Table 2 quantitatively verified the proposed method outperformed in image fidelity and smoothness. Noticeably, the proposed method accurately estimated ρ_e and Z maps (see Table 1), of which the relative error is consistently smaller than 0.24 for ρ_e map and 0.59 for Z map.

B. MULTI-ENERGY PHANTOM STUDY

We also scanned Gammex multi-energy phantom model 1472 (Gammex Inc., Middleton, WI). The phantom includes 15 inserts with various materials. The material list and the reference value of ρ_e and Z are shown in Table 3, where the reference Z value are calculated with Mayneord's power-law method ($Z = \sqrt[n]{\sum_i \alpha_i Z_i^n}$) with $n = 2.94$, where Z_i is the

atomic number of element i and α_i is the fraction of the total number of electrons associated with element i [36]. Calcium and CT solid water were selected as basis materials. Fig. 3 illustrates the decomposed material images and maps of ρ_e and Z . Estimation accuracy and image quality assessments are shown in Tables 3 and 4 respectively.

It is obvious, this study is more noisy than the previous one because of larger phantom size, but the proposed method stills works well for the severe scenario (see Fig. 3). Moreover, the estimation accuracy of the proposed method is still reasonable. The relative error is consistently smaller than 0.27 for ρ_e map and 0.48 for Z map. Both phantom studies consistently demonstrate the superiority of the proposed method in noise reduction, and accurate estimation.

C. PATIENT STUDY

For the patient experiment shown in Fig. 4, the two basis materials are selected as cortical bone and soft tissue. From the bone comparisons, we can figure out the proposed method well preserves the edges and concentration, but the direct method performs inferior. From the soft tissue images, we can also find the direct decomposition image suffers from obvious noise, but the proposed method can effectively suppress it. The same conclusion can also be made from ρ_e and

Z comparisons.

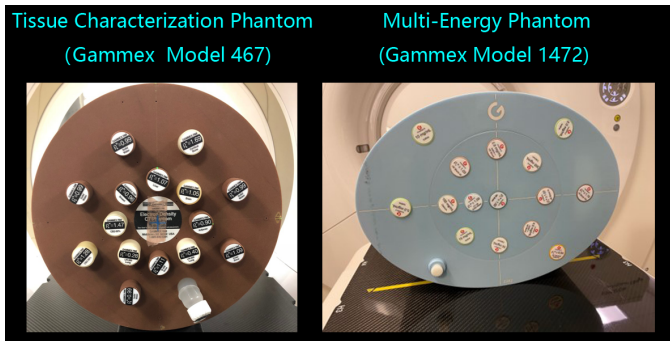


FIGURE 1. Phantom illustrations.

IV. DISCUSSIONS

Conventionally, the estimation of ρ_e and Z maps is based on the decomposed material images from DECT, i.e., the estimation and decomposition are independent processes. However, in this work, we effectively combined the two steps within an optimization model and simultaneously achieved material composition, ρ_e and Z maps. The theoretical superiority lies in two aspects. First, the searched-for material composition, ρ_e and Z maps are efficaciously connected by the proposed model. During the iterative solution process, each map is alternatively updated according to the constraints from the others, i.e., mutual correction. Thus, all the maps are continuously optimized in a consistent manner. Second, we introduced smoothness mechanism for each inverse solution to overcome the illposedness of both decomposition and estimation processes. Thus, the noise can be remarkably suppressed for all the searched-for maps.

In tissue characterization phantom study, results in Tables 1 and 2 demonstrate the improved ρ_e and Z estimation accuracy of the proposed method for most of the materials, especially for high Z materials, such as cortical bone, CaCO_3 , and inner bone. Although the estimation performance of the proposed method is very similar with the image-based method for low Z materials, i.e., liver, brain, water, breast, adipose and lung, the standard deviation of the proposed method is much smaller, which reveals the effectiveness of noise suppression and smoothness mechanism of the proposed method. In multi-energy phantom study, although the noise is severer than the previous study, the proposed method can still obtain reasonable ρ_e and Z estimation results (see Tables 4 and 5) compared with the image-based method. Remarkably, the standard deviation of Z estimation by the proposed method is consistently smaller than the image-based method for all the materials. Same conclusion can also be drawn from ρ_e estimation with low Z materials, such as blood, brain, water and adipose. In addition, for both studies, the image quality assessment indexes of PSNR, NMAD, and SSIM shown in Tables 3 and 5 confirm the superior performance of the proposed method in signal to noise ratio and image structural similarity. It is worth noting that

both methods cannot accurately estimate all the materials, which is owing to the decomposition rationale. In this inverse problem, we collected two data sets from DECT scan, but we need to estimate ρ_e and Z maps for 13 or 16 materials, which is essentially under-determined. Actually, each map is expressed by the combination of the two selected basis materials. This linear representation mechanism inevitably limits the estimation accuracy of some specific materials. To further overcome the limitation, we will improve and develop the proposed method to a multiple-basis-material based version. In this way, each material can find its optimal expression from the large basis material pool.

Although the proposed method has some superiority and novelty in terms of theoretical model, it still has some limitations confining its direct application. First, there are a lot of parameters need to be determined by an automatic selection strategy. However, up to now, we just experimentally optimized and chose them, but we still did not have some clear rules or indicators. Basically, the regularization and relaxation parameters highly rely on the quality of acquired data and specific structures of searched-for maps. If the collected data is very noisy, then we may prefer larger smoothness parameters. However, if the searched-for maps contain very fine structures, we may sacrifice the smoothness to preserve image details. To improve the application value, we need to provide experimental parameters for common scenarios, propose general rules for parameter optimization, and further develop robust auto-selection strategy.

V. CONCLUSIONS

In this work, we propose a one-step iterative estimation method for ρ_e and Z maps with multi-domain gradient L_0 -norm minimization. The employed gradient L_0 -norm, as a smoothness regularizer, directly and effectively suppresses noise and reduces artifact in the decomposition domain. The proposed method does not rely on X-ray spectra, i.e., extra spectrum estimations can be avoided. Moreover, it can be accelerated by parallel computing and converge very fast (all the experiments can be finished in 2 minutes with single GPU (NVIDIA GeForce GTX 960M)). Both phantom and patient studies demonstrate the superiority of the proposed method in material-selective reconstruction, noise removal, artifacts reduction and accurate estimation of ρ_e and Z maps.

The clinical meaning of this work lies in more accurate estimation of Z and ρ_e , which can be further employed for SPR calculation for proton therapy [6]. Moreover, we can synthesize monoenergetic images for dose verification or ROI contrast enhancement. In the future, we will extend this method for multiple material based decomposition, and develop automatic parameter optimization strategies.

ACKNOWLEDGEMENT

This research is supported in part by the National Cancer Institute of the National Institutes of Health under Award Number R01CA215718.

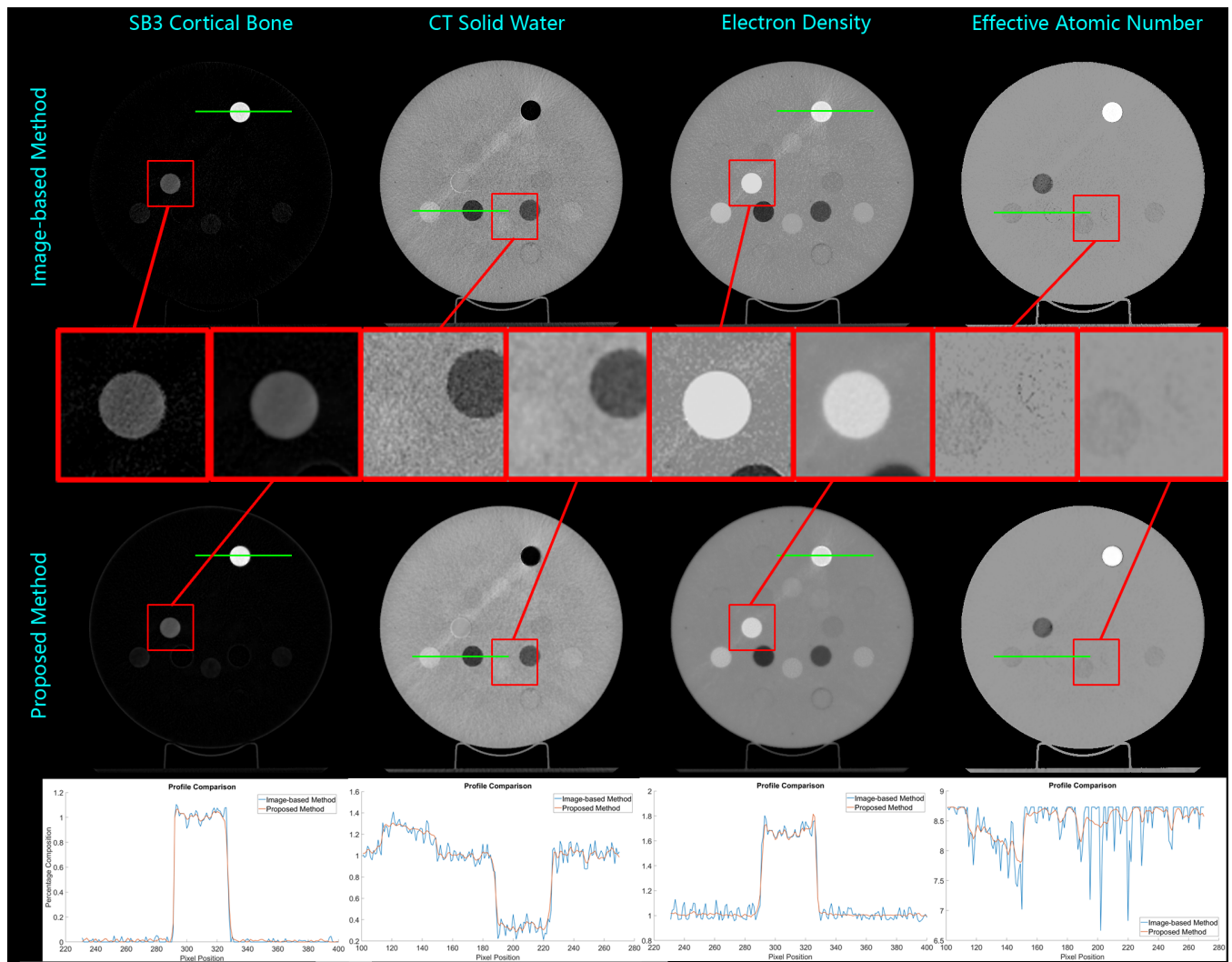


FIGURE 2. Material decomposition of tissue characterization phantom study by using classic image-based method and the proposed method.

REFERENCES

- [1] X. Zhang, Y. Li, X. Pan, L. Xiaoqiang, R. Mohan, R. Komaki, J. D. Cox, and J. Y. Chang, "Intensity-modulated proton therapy reduces the dose to normal tissue compared with intensity-modulated radiation therapy or passive scattering proton therapy and enables individualized radical radiotherapy for extensive stage iiib non-small-cell lung cancer: a virtual clinical study," *International Journal of Radiation Oncology* Biology* Physics*, vol. 77, no. 2, pp. 357–366, 2010.
- [2] H. Paganetti, "Range uncertainties in proton therapy and the role of monte carlo simulations," *Physics in Medicine & Biology*, vol. 57, no. 11, p. R99, 2012.
- [3] U. Schneider, E. Pedroni, and A. Lomax, "The calibration of ct hounsfield units for radiotherapy treatment planning," *Physics in Medicine & Biology*, vol. 41, no. 1, p. 111, 1996.
- [4] W. Schneider, T. Bortfeld, and W. Schlegel, "Correlation between ct numbers and tissue parameters needed for monte carlo simulations of clinical dose distributions," *Physics in Medicine & Biology*, vol. 45, no. 2, p. 459, 2000.
- [5] C.-W. Chang, S. Huang, J. Harms, J. Zhou, R. Zhang, A. Dhabaan, R. Slopsma, M. Kang, T. Liu, M. McDonald *et al.*, "A standardized commissioning framework of monte carlo dose calculation algorithms for proton pencil beam scanning treatment planning systems," *Medical physics*, vol. 47, no. 4, pp. 1545–1557, 2020.
- [6] J. Harms, Y. Lei, T. Wang, M. McDonald, B. Ghavidel, W. Stokes, W. J. Curran, J. Zhou, T. Liu, and X. Yang, "Cone-beam ct-derived relative stopping power map generation via deep learning for proton radiotherapy," *Medical Physics*, vol. 47, no. 9, pp. 4416–4427, 2020.
- [7] E. Bär, A. Lalonde, G. Royle, H.-M. Lu, and H. Bouchard, "The potential of dual-energy ct to reduce proton beam range uncertainties," *Medical physics*, vol. 44, no. 6, pp. 2332–2344, 2017.
- [8] J. Zhu and S. N. Penfold, "Dosimetric comparison of stopping power calibration with dual-energy ct and single-energy ct in proton therapy treatment planning," *Medical physics*, vol. 43, no. 6Part1, pp. 2845–2854, 2016.
- [9] M. Yang, G. Virshup, J. Clayton, X. R. Zhu, R. Mohan, and L. Dong, "Theoretical variance analysis of single-and dual-energy computed tomography methods for calculating proton stopping power ratios of biological tissues," *Physics in Medicine & Biology*, vol. 55, no. 5, p. 1343, 2010.
- [10] A. E. Bourque, J.-F. Carrier, and H. Bouchard, "A stoichiometric calibration method for dual energy computed tomography," *Physics in Medicine & Biology*, vol. 59, no. 8, p. 2059, 2014.
- [11] E. Bär, A. Lalonde, R. Zhang, K.-W. Jee, K. Yang, G. Sharp, B. Liu, G. Royle, H. Bouchard, and H.-M. Lu, "Experimental validation of two dual-energy ct methods for proton therapy using heterogeneous tissue samples," *Medical physics*, vol. 45, no. 1, pp. 48–59, 2018.
- [12] Y. Xie, C. Ainsley, L. Yin, W. Zou, J. McDonough, T. D. Solberg, A. Lin, and B.-K. K. Teo, "Ex vivo validation of a stoichiometric dual energy ct proton stopping power ratio calibration," *Physics in Medicine & Biology*, vol. 63, no. 5, p. 055016, 2018.
- [13] C. Maaß, M. Baer, and M. Kachelrieß, "Image-based dual energy ct using

TABLE 1. Electron density and effective atomic number comparisons of tissue characterization phantom study.

		Reference Value	Electron density			Reference Value	Effective atomic number		
			Mean Value	Standard Deviation	Relative Error		Mean Value	Standard Deviation	Relative Error
SB3 Cortical Bone	Image-based Method	1.6900	1.6686	0.0454	0.0127	14.1400	14.2982	0.1256	0.0112
	Proposed Method		1.6754	0.0489	0.0086		14.1683	0.3024	0.0020
CB2 - 50% CaCO3	Image-based Method	1.4700	1.5850	0.0026	0.0782	12.9800	5.2557	0.8418	0.5951
	Proposed Method		1.5788	0.0223	0.0740		5.4246	0.5667	0.5821
CB2 - 30% CaCO3	Image-based Method	1.2800	1.3637	0.0150	0.0654	11.3900	8.1450	0.3151	0.2849
	Proposed Method		1.3524	0.0242	0.0566		8.1684	0.1480	0.2828
B200 Bone Mineral	Image-based Method	1.1000	1.1692	0.0181	0.0629	10.9000	8.1371	0.3812	0.2535
	Proposed Method		1.1647	0.0181	0.0588		8.1764	0.1573	0.2499
IB Inner Bone	Image-based Method	1.0900	1.1599	0.0193	0.0641	10.9000	8.2477	0.3217	0.2433
	Proposed Method		1.1550	0.0185	0.0596		8.2766	0.1265	0.2407
LV1 Liver	Image-based Method	1.0600	1.1224	0.0601	0.0588	8.1100	8.6285	0.1897	0.0639
	Proposed Method		1.1080	0.0215	0.0453		8.6506	0.0877	0.0667
BRN-SR2 Brain	Image-based Method	1.0400	1.0633	0.0553	0.0224	6.3100	8.6457	0.1744	0.3702
	Proposed Method		1.0520	0.0123	0.0116		8.6665	0.0623	0.3735
True Water	Image-based Method	1.0000	0.9955	0.0514	0.0045	7.4200	8.6333	0.2084	0.1635
	Proposed Method		0.9833	0.0274	0.0167		8.6548	0.0951	0.1664
CT Solid Water	Image-based Method	0.9900	1.0125	0.0485	0.0228	8.1100	8.6099	0.2102	0.0616
	Proposed Method		1.0053	0.0173	0.0155		8.6305	0.0849	0.0642
BR-12 Breast	Image-based Method	0.9600	0.9783	0.0481	0.0190	7.2400	8.6044	0.2092	0.1885
	Proposed Method		0.9736	0.0109	0.0141		8.6268	0.0721	0.1915
AP6 Adipose	Image-based Method	0.9300	0.9554	0.0517	0.0273	6.4000	8.6161	0.2115	0.3463
	Proposed Method		0.9478	0.0100	0.0192		8.6396	0.0744	0.3499
LN-450 Lung	Image-based Method	0.4400	0.5191	0.0495	0.1798	7.8400	8.5520	0.3933	0.9908
	Proposed Method		0.5278	0.0312	0.1995		8.5893	0.1117	0.0956
LN-300 Lung	Image-based Method	0.2900	0.3495	0.0516	0.2053	7.8600	8.5076	0.5974	0.0824
	Proposed Method		0.3582	0.0311	0.2353		8.5691	0.1154	0.0902

TABLE 2. Image quality assessments of tissue characterization phantom study.

	Electron Density		
	PSNR	NMAD	SSIM
Image-based Method	39.6855	0.0514	0.9841
Proposed Method	42.0432	0.0383	0.9976
	Effective Atomic Number		
	PSNR	NMAD	SSIM
Image-based Method	27.5920	0.1660	0.9859
Proposed Method	27.7670	0.1645	0.9944

optimized precorrection functions: A practical new approach of material decomposition in image domain,” *Medical physics*, vol. 36, no. 8, pp. 3818–3829, 2009.

[14] T. G. Flohr, C. H. McCollough, H. Bruder, M. Petersilka, K. Gruber, C. Süß, M. Grasruck, K. Stierstorfer, B. Krauss, R. Raupach et al., “First performance evaluation of a dual-source CT (DSCT) system,” *European radiology*, vol. 16, no. 2, pp. 256–268, 2006.

[15] P. Stenner, T. Berkus, and M. Kachelrieß, “Empirical dual energy calibration (edec) for cone-beam computed tomography,” *Medical physics*, vol. 34, no. 9, pp. 3630–3641, 2007.

[16] I. A. Elbakri and J. A. Fessler, “Statistical image reconstruction for polyenergetic X-ray computed tomography,” *IEEE transactions on medical imaging*, vol. 21, no. 2, pp. 89–99, 2002.

[17] Q. Xu, X. Mou, S. Tang, W. Hong, Y. Zhang, and T. Luo, “Implementation of penalized-likelihood statistical reconstruction for polychromatic dual-energy CT,” in *SPIE Medical Imaging*. International Society for Optics and Photonics, 2009, pp. 72 585I–72 585I.

[18] C. Maaß, R. Grimmer, and M. Kachelrieß, “Dual energy CT material decomposition from inconsistent rays (MDIR),” in *2009 IEEE Nuclear*

Science Symposium Conference Record (NSS/MIC). IEEE, 2009, pp. 3446–3452.

[19] T. Niu, X. Dong, M. Petrongolo, and L. Zhu, “Iterative image-domain decomposition for dual-energy CT,” *Medical physics*, vol. 41, no. 4, p. 041901, 2014.

[20] R. E. Alvarez and A. Macovski, “Energy-selective reconstructions in x-ray computerized tomography,” *Physics in medicine and biology*, vol. 21, no. 5, p. 733, 1976.

[21] L. Lehmann, R. Alvarez, A. Macovski, W. Brody, N. Pelc, S. J. Riederer, and A. Hall, “Generalized image combinations in dual kvp digital radiography,” *Medical physics*, vol. 8, no. 5, pp. 659–667, 1981.

[22] K. Mei, S. Ehn, M. Oechsner, F. K. Kopp, D. Pfeiffer, A. A. Fingerle, F. Pfeiffer, S. E. Combs, J. J. Wilkens, E. J. Rummeny et al., “Dual-layer spectral computed tomography: measuring relative electron density,” *European radiology experimental*, vol. 2, no. 1, pp. 1–9, 2018.

[23] A. N. Tikhonov, V. I. Arsenin, and F. John, *Solutions of ill-posed problems*. Winston Washington, DC, 1977, vol. 14.

[24] L. Rudin, S. Osher, and E. Fatemi, “Nonlinear total variation based noise removal algorithms,” *Physica D*, vol. 60, no. 1, pp. 259–268, 1992.

[25] L. Rudin and S. Osher, “Total variation based image restoration with free local constraints,” in *Image Processing, 1994. Proceedings. ICIP-94., IEEE International Conference*. IEEE, 1994, pp. 31–35.

[26] S. Osher, A. Solé, and L. Vese, “Image decomposition and restoration using total variation minimization and the H1,” *Multiscale Modeling & Simulation*, vol. 1, no. 3, pp. 349–370, 2003.

[27] T. Blumensath, M. Yaghoobi, and M. E. Davies, “Iterative hard thresholding and l0 regularization,” in *2007 IEEE International Conference on Acoustics, Speech and Signal Processing-ICASSP’07*, vol. 3. IEEE, 2007, pp. III–877.

[28] R. Peharz and F. Pernkopf, “Sparse nonnegative matrix factorization with l0-constraints,” *Neurocomputing*, vol. 80, pp. 38–46, 2012.

[29] L. Xu, C. Lu, Y. Xu, and J. Jia, “Image smoothing via l0 gradient minimization,” vol. 30, no. 6, p. 174, 2011.

[30] L. Xu, S. Zheng, and J. Jia, “Unnatural l0 sparse representation for natural image deblurring,” in *Proceedings of the IEEE conference on computer vision and pattern recognition*, 2013, pp. 1107–1114.

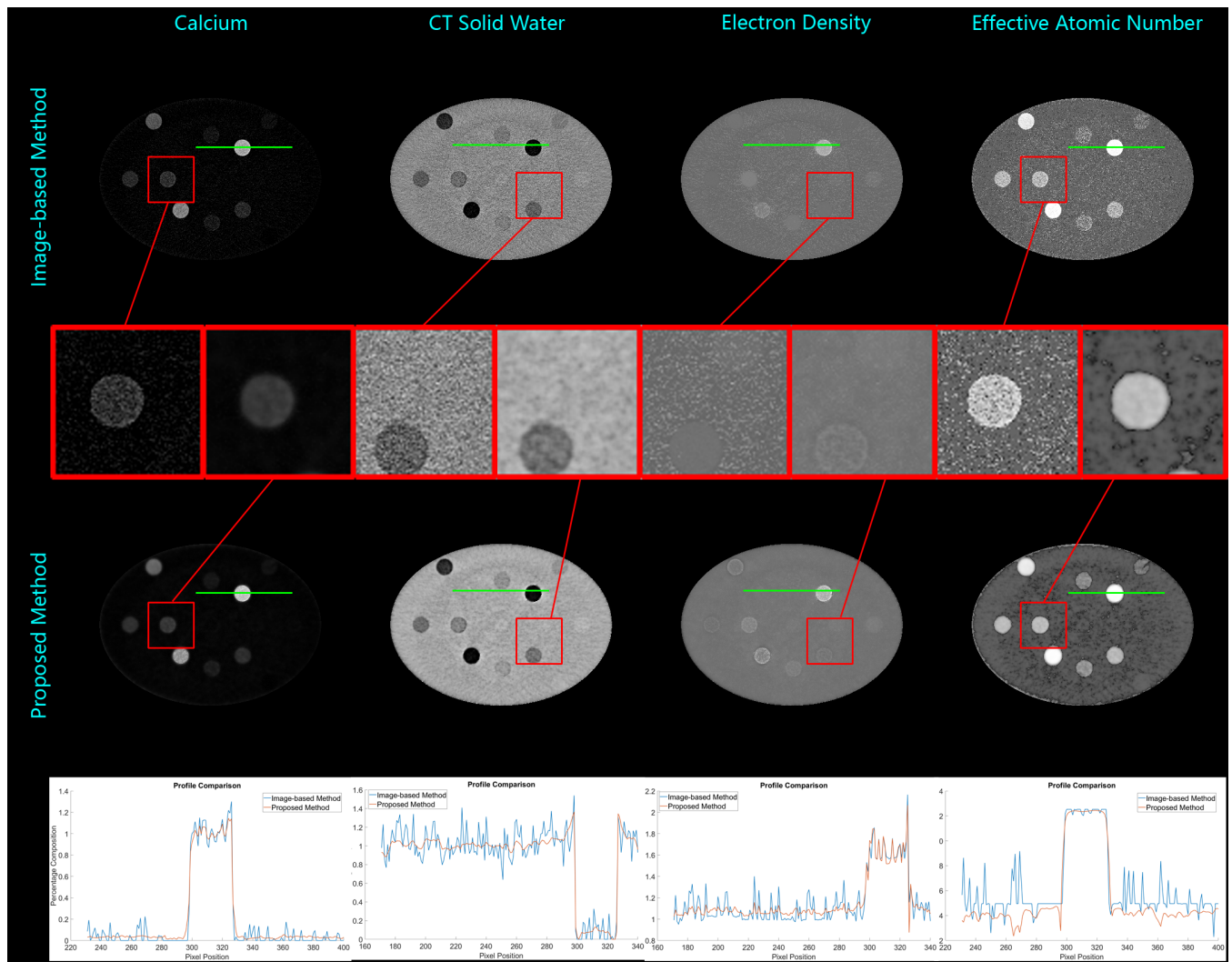


FIGURE 3. Material decomposition of multi-energy phantom study by using classic image-based method and the proposed method.

- [31] B. Heismann, J. Leppert, and K. Stierstorfer, "Density and atomic number measurements with spectral x-ray attenuation method," *Journal of applied physics*, vol. 94, no. 3, pp. 2073–2079, 2003.
- [32] P. Granton, S. Pollmann, N. Ford, M. Drangova, and D. Holdsworth, "Implementation of dual-and triple-energy cone-beam micro-ct for postreconstruction material decomposition," *Medical physics*, vol. 35, no. 11, pp. 5030–5042, 2008.
- [33] Q. Huynh-Thu and M. Ghanbari, "Scope of validity of PSNR in image/video quality assessment," *Electronics letters*, vol. 44, no. 13, pp. 800–801, 2008.
- [34] Y. Zhu, M. Zhao, Y. Zhao, H. Li, and P. Zhang, "Noise reduction with low dose CT data based on a modified ROF model," *Optics express*, vol. 20, no. 16, pp. 17 987–18 004, 2012.
- [35] Z. Wang, A. C. Bovik, H. R. Sheikh, and E. P. Simoncelli, "Image quality assessment: from error visibility to structural similarity," *IEEE transactions on image processing*, vol. 13, no. 4, pp. 600–612, 2004.
- [36] C. J. Schaeffer, S. M. Leon, C. A. Olguin, and M. M. Arreola, "Accuracy and reproducibility of effective atomic number and electron density measurements from sequential dual energy ct," *Medical Physics*, 2021.

...

TABLE 3. Electron density and effective atomic number comparisons of multi-energy phantom study.

		Reference Value	Electron density			Effective atomic number			
			Mean Value	Standard Deviation	Relative Error	Reference Value	Mean Value	Standard Deviation	Relative Error
Calcium 300 mg/mL	Image-based Method	1.4500	1.6441	0.0991	0.1338	12.2100	12.3824	0.2364	0.0141
	Proposed Method		1.6504	0.1117	0.1382		12.3724	0.0723	0.0133
Calcium 100mg/mL	Image-based Method	1.1900	1.2225	0.0144	0.0273	9.8700	9.0083	1.3748	0.0873
	Proposed Method		1.2254	0.0461	0.0297		9.2112	0.3935	0.0667
Calcium 50mg/mL	Image-based Method	1.1300	1.1469	0.0268	0.0150	8.8000	6.7705	2.1205	0.2306
	Proposed Method		1.1489	0.0390	0.0167		7.1021	0.8801	0.1929
Iodine+HE Blood 4.0mg/mL	Image-based Method	1.0400	1.0708	0.0184	0.0296	9.3400	8.7101	1.8018	0.0674
	Proposed Method		1.0750	0.0482	0.0337		9.0606	0.4016	0.0299
Iodine+HE Blood 2.0mg/mL	Image-based Method	1.0400	1.0594	0.0324	0.0187	8.4700	6.4151	2.1010	0.2426
	Proposed Method		1.0606	0.0362	0.0198		6.6707	0.8492	0.2124
Iodine 15mg/mL	Image-based Method	1.0100	1.2650	0.1241	0.2525	12.4900	12.3921	0.2761	0.0078
	Proposed Method		1.2758	0.1302	0.2632		12.3529	0.1122	0.0110
Iodine 10mg/mL	Image-based Method	1.0100	1.0991	0.0116	0.0883	11.2500	11.4684	0.5295	0.0194
	Proposed Method		1.1096	0.0405	0.0986		11.4268	0.1869	0.0157
Iodine 5.0mg/mL	Image-based Method	1.0000	1.0425	0.0107	0.0425	9.6500	9.0884	1.2136	0.0582
	Proposed Method		1.0491	0.0382	0.0491		9.2008	0.3066	0.0466
Iodine 2.0mg/mL	Image-based Method	1.0000	1.0282	0.0272	0.0282	8.3700	5.8977	1.8065	0.2954
	Proposed Method		1.0302	0.0284	0.0302		5.6042	1.1703	0.3304
HE Blood 100	Image-based Method	1.1000	1.1309	0.0779	0.0281	7.2600	4.9398	1.1733	0.3196
	Proposed Method		1.1288	0.0397	0.0262		4.0157	0.6750	0.4469
HE Blood 70	Image-based Method	1.0700	1.1143	0.0879	0.0414	7.3400	5.1408	1.4103	0.2996
	Proposed Method		1.1122	0.0439	0.0394		3.9316	0.7626	0.4644
HE Blood 40	Image-based Method	1.0300	1.0795	0.0863	0.0480	7.4200	5.1449	1.3658	0.3066
	Proposed Method		1.0777	0.0432	0.0463		3.8966	0.8010	0.4749
HE Brain	Image-based Method	1.0200	1.0981	0.1185	0.0765	7.4200	5.0935	1.2363	0.3135
	Proposed Method		1.0957	0.0615	0.0743		4.0788	0.7598	0.4503
True Water	Image-based Method	1.0000	1.0431	0.0762	0.0431	7.4200	4.9276	1.1237	0.3359
	Proposed Method		1.0404	0.0380	0.0404		4.0875	0.5796	0.4491
CT HE Solid Water	Image-based Method	1.0000	1.0578	0.0954	0.0578	7.2400	5.0767	1.1944	0.2988
	Proposed Method		1.0570	0.0493	0.0570		4.0840	0.6466	0.4359
HE General Adipose	Image-based Method	0.9400	1.0417	0.1023	0.1082	6.4400	4.8484	0.6123	0.2471
	Proposed Method		1.0411	0.0551	0.1076		4.7153	0.2434	0.2678

TABLE 4. Image quality assessments of multi-energy phantom study.

	Electron Density		
	PSNR	NMAD	SSIM
Image-based Method	36.0653	0.0703	0.9891
Proposed Method	36.7651	0.0706	0.9906
	Effective Atomic Number		
	PSNR	NMAD	SSIM
Image-based Method	29.3859	0.2069	0.9785
Proposed Method	29.4807	0.2046	0.9830

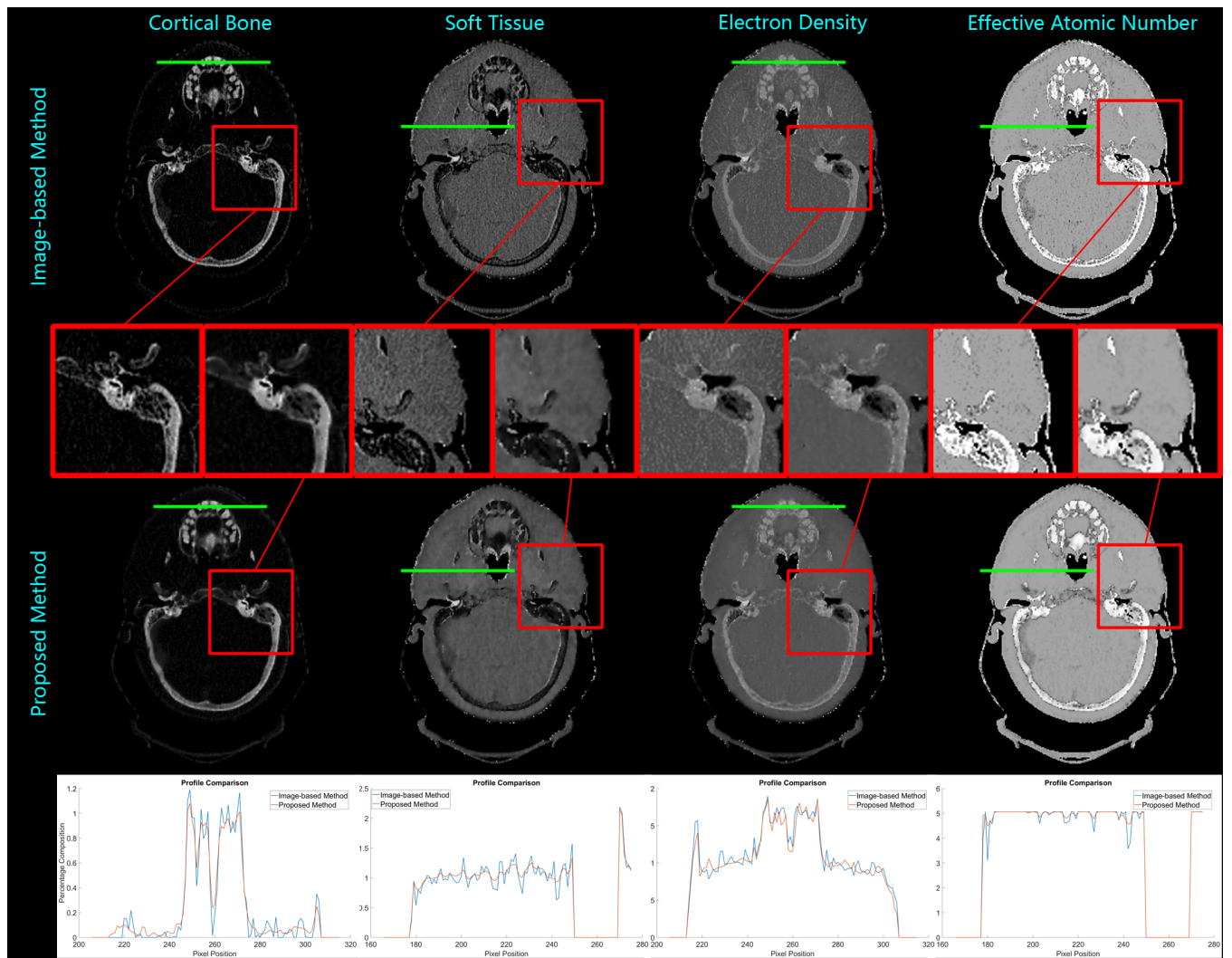


FIGURE 4. Material decomposition of patient study by using classic image-based method and the proposed method.